Neuron

Supplemental Information

White-Matter Tract Connecting Anterior Insula to Nucleus Accumbens Correlates with Reduced Preference for Positively Skewed Gambles

Josiah K. Leong, Franco Pestilli, Charlene C. Wu, Gregory R. Samanez-Larkin, and Brian Knutson

Supplemental Information

Supplemental Data

Supplemental Experimental Procedures

Supplemental Data
Figure S1. Related to Figure 1.

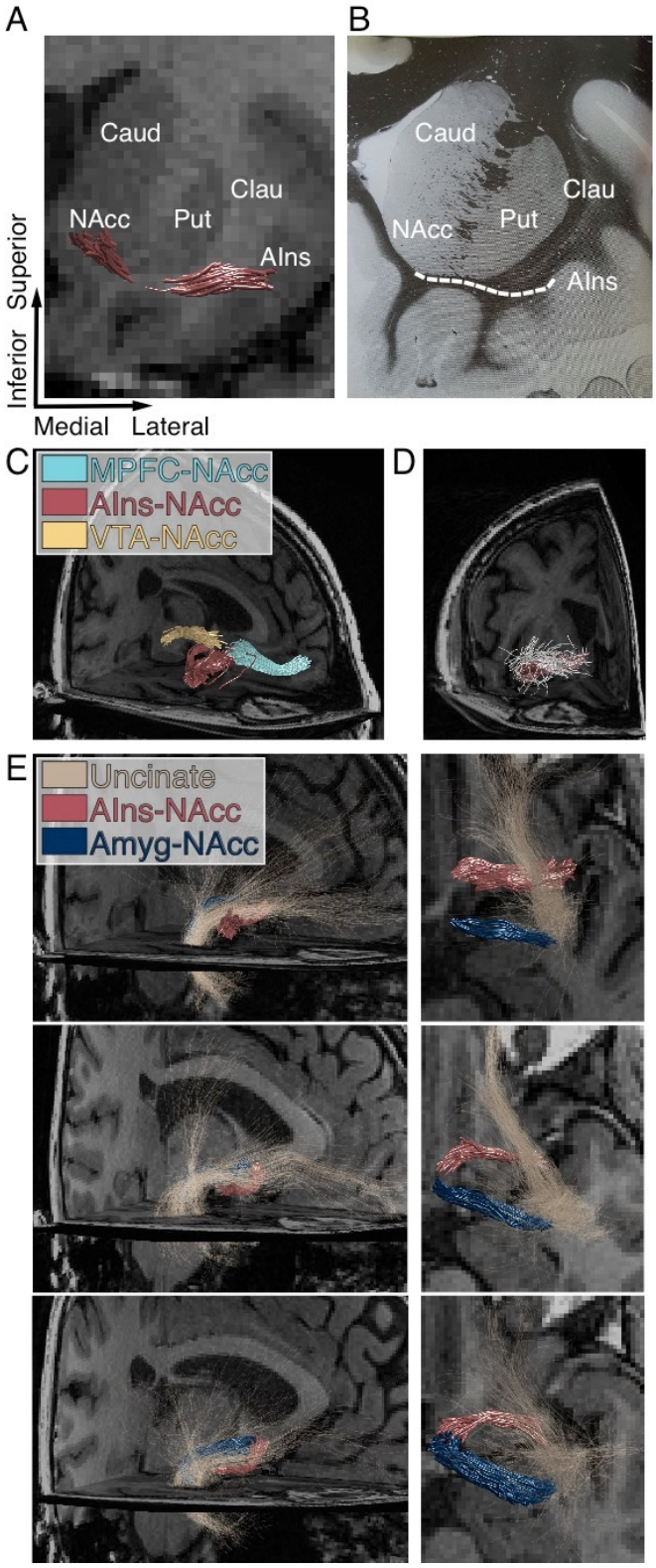

(A) AIns to NAcc tract traverses subcaudate white matter inferior to the claustrum and putamen, intersecting laterally with the uncinate fasciculus. Controlling for coherence of crossing fibers did not change the observed relations between AIns-NAcc tract coherence and age or behavior (see *Table S2*).
(B) Myelin-stained coronal slice of right hemisphere at level of the caudate head (NAcc=nucleus accumbens, Caud=caudate, Clau=claustrum, AIns=anterior insula, Put=putamen, adapted from Mai, Assheuer, and Paxinos, 1997).
(C) Reproduction of **Figure 1A** with the AIns-NAcc tract prior to removing outliers, as described in *Experimental Procedures*.
(D) Path-neighborhood fascicles from the whole-brain connectome for a representative subject's right AIns-NAcc tract. The fascicles which comprised the AIns-NAcc tract were included with these fascicles (as depicted) in the full model to predict raw diffusion signal. The "virtually lesioned" model included only the path-neighborhood fascicles. Root mean squared error of the predicted diffusion signal was compared to test the strength of evidence for the tract (see *Supplemental Experimental Procedures*).
(E) Sagittal and axial cross sections of three representative subjects' right AIns-NAcc tract, uncinate fasciculus, and amygdala-NAcc tract. Coherence of these tracts were entered as covariates of no interest in all regressions involving the AIns-NAcc tract (see *Table S3*). The AIns-NAcc tract passes ventrally through the uncinate fasciculus along the lateral-medial axis, and the pathways share a proportion of their voxels, (computed within subject then averaged between subjects: right mean=0.45, standard deviation=0.18, range=0.00-0.71; left mean=0.36, standard deviation=0.14, range=0.01-0.65).

Figure S2. Related to Figure 2.

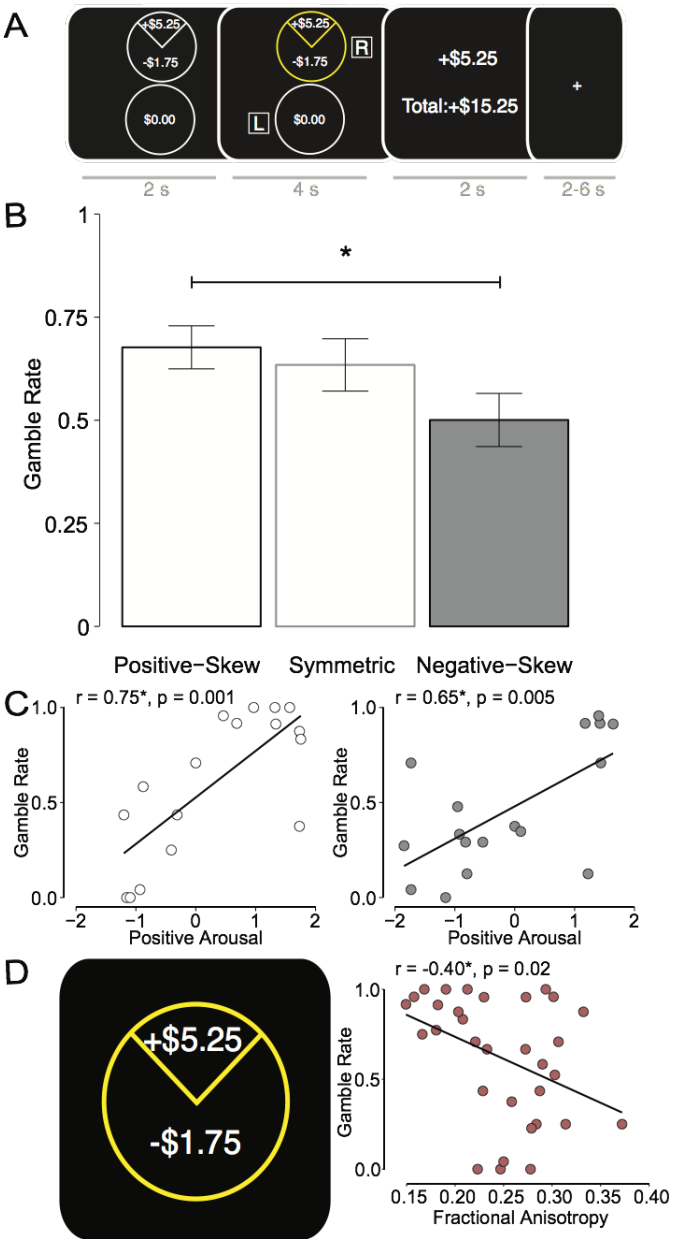

(A) Gambling task trial structure. Subjects passively viewed two gamble options (2 s), then chose between the gambles (4 s), saw the gamble outcome (2 s), and then fixated for a variable 2-6 s inter-trial interval until the next trial began (see *Experimental Procedures*).

(B) Risk seeking rate for each gamble condition. Mean gamble rate and standard error were computed for subjects who did not always seek or avoid risk for any gamble condition (n=20). Positively skewed gambles were preferred to negatively skewed gambles (paired t(19)=2.13, p=0.047).

(C) Subjects (n=17) rated each gamble type on a 7-point Likert scale for evoked valence (negative-positive) and arousal (low-high), after performing the gambling task (data loss due to a technical difficulty). Ratings were mean-deviated within subject, plotted along the two dimensions and rotated 45 degrees to derive affective measures of positive and negative arousal. Positive arousal ratings towards positively and negatively skewed gambles were highly correlated with risk seeking for each of those gambles (positive-skew: **β**=0.75, t(15)=4.40, p=0.0005; negative-skew: **β**=0.65, t(15)=3.32, p=0.005).

(D) Individual differences in right AIns-NAcc tract coherence was associated with decreased preference for positively skewed gambles (**β**=-0.40, t(30)=-2.38, p=0.02; see also *Table S1*).

Figure S3. Related to Figure 2.

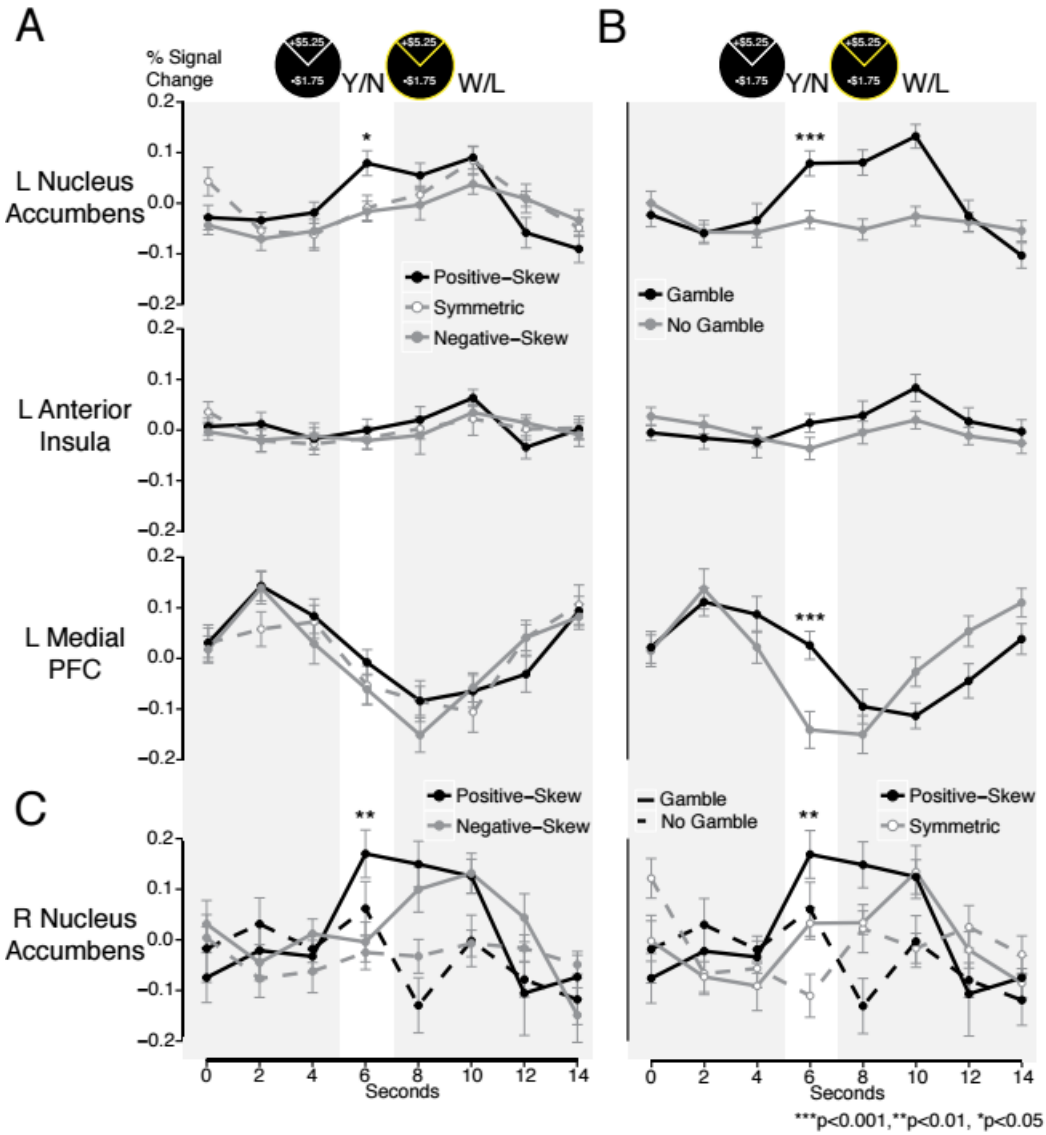

(A) Left hemisphere activity time courses showed a similar pattern of functional activity in each volume of interest (VOI) as the right hemisphere, with the same significant main effects. Presentation of positively skewed gambles elicited greatest NAcc activity (positive-skew > symmetric: paired t(31)=2.87, p=0.007; positive-skew > negative-skew: paired t(31)=3.02, p=0.005).

(B) Similar to right hemisphere, left NAcc and MPFC activity were greater prior to gamble acceptance than rejection across conditions (NAcc: paired t(31)=3.54, p=0.001; MPFC: paired t(31)=3.78, p=0.001).

(C) Right NAcc activity was greater during choice for accepted positive-skew than accepted negative-skew and accepted symmetric gambles (positive > negative: t(26)=3.07, p=0.005; positive > symmetric: t(28)=3.31, p=0.003).

Figure S4. Related to Figure 3.

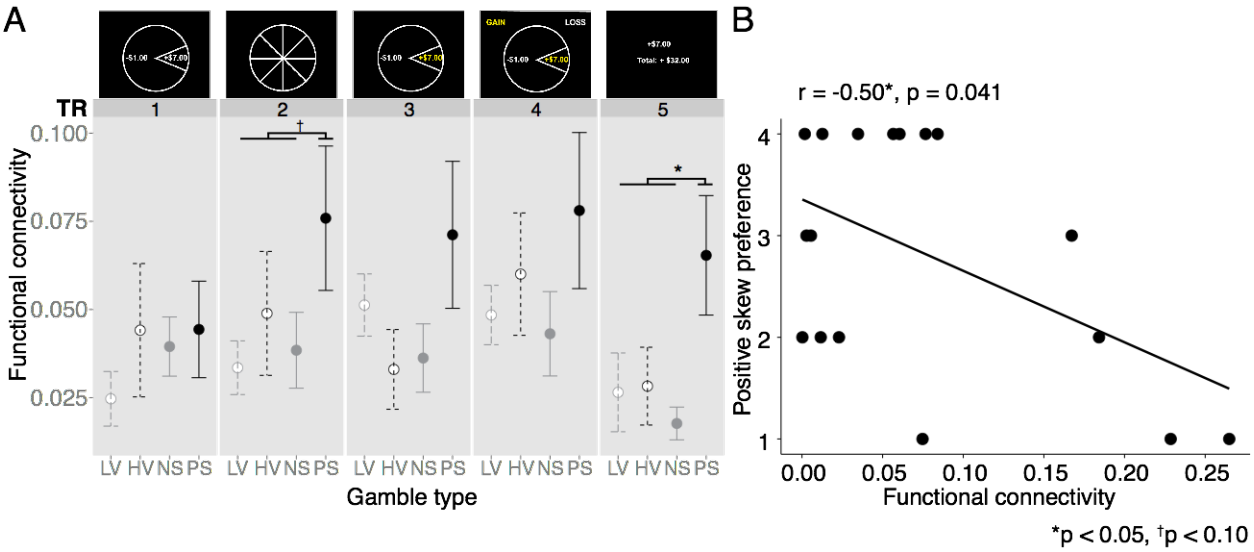

Confirmatory analyses were performed on previously published FMRI data (see Wu et al., 2011 for full experimental procedures). In that study, subjects (N=17) passively viewed gambles and their outcomes during FMRI. Subjects encountered four gamble types which were equated for expected value but differed in skewness: "Low-Variance" (LV), which yielded equal probability (50%) of winning or losing $1.00; "High-Variance" (HV), which yielded equal probability (50%) of winning or losing $2.75; "Negative-Skew" (NS), which yielded a low probability (12.5%) of losing a large amount (-$7.00) paired with a high probability (87.5%) of winning a small amount (+$1.00); "Positive-Skew" (PS), which yielded a low probability (12.5%) of winning a large amount (+ $7.00) paired with a high probability (87.5%) of losing a small amount (-$1.00). During each trial, subjects were presented a single gamble (2 s), saw the gamble spin randomly (2 s), saw the gamble outcome (2 s), responded to confirm they saw the outcome (2 s), and viewed their cumulative earnings for the task (2 s). After the experiment, subjects ranked the four gamble types in the order they would prefer to play them again. BOLD activity time courses were extracted from right hemisphere AIns and NAcc VOIs and lagged 6 seconds to account for the hemodynamic lag. The "functional connectivity" between the AIns and NAcc for each subject was assessed by performing simple linear regression between the two VOIs' activity for every phase of the trial (corresponding to volume acquisitions) and for each gamble type. The variance explained in the regression (r^2) was then averaged across subjects to extract a measure of functional connectivity for every trial phase and for each gamble type.

(A) Right AIns-NAcc functional connectivity was greater when subjects saw positively skewed gambles spin relative to all other gamble types with marginal significance (paired $t(16)=1.75$, $p<0.10$). Functional connectivity was also greatest while subjects viewed the outcomes of positively skewed gambles, relative to all other gambles (paired $t(16)=2.64$, $p=0.018$).

(B) Right AIns-NAcc functional connectivity while subjects saw the positively skewed gamble spin was used in individual difference analyses, and was associated with decreased preference for positively skewed gambles in post-scan ratings, ($\beta=0.50$, $t(15)=2.24$, $p=0.04$). FMRI data from the current study were analyzed the same way. Right AIns-NAcc functional connectivity before subjects chose to accept or reject gambles was greater for positively and negatively skewed gambles than for symmetric gambles (paired $t(31)=2.01$, $p=0.053$). In addition, right AIns-NAcc tract coherence was correlated with right AIns-NAcc functional connectivity when subjects first saw the prospective gambles for all gamble types (positive-skew: $\beta=0.47$, $t(30)=2.92$, $p=0.007$; symmetric: $\beta=0.41$, $t(30)=2.48$, $p=0.019$; negative-skew: $\beta=0.36$, $t(30)=2.13$, $p=0.041$; all coefficient estimates are standardized).

Table S1. Related to Figure 2.
An omnibus repeated-measures multivariate analysis of variance was performed by regressing the risk seeking rate for all three gamble conditions against all three bilateral tracts (six total tracts). This revealed a significant tract by gamble condition interaction for the AIns-NAcc tract bilaterally, and a significant difference in risk seeking by gamble condition. The significant interactions were examined in pairwise correlations described in the main text.

Variable	**Pillai's Trace**	**F-test**
AIns - NAcc (R)	0.265	F(1,25)=1.744, p=0.199
AIns - NAcc (L)	0.002	F(1,25)=0.011, p=0.916
MPFC - NAcc (R)	0.095	F(1,25)=0.626, p=0.437
MPFC - NAcc (L)	0.006	F(1,25)=0.042, p=0.840
VTA - NAcc (R)	0.044	F(1,25)=0.290, p=0.595
VTA - NAcc (L)	0.044	F(1,25)=0.289, p=0.596
Gamble condition	0.622	F(2,50)=4.016*, p=0.024
AIns - NAcc (R) * gamble condition	0.634	F(2,50)=4.097*, p=0.023
AIns - NAcc (L) * gamble condition	0.726	F(2,50)=4.688*, p=0.014
MPFC - NAcc (R) * gamble condition	0.012	F(2,50)=0.078, p=0.925
MPFC - NAcc (L) * gamble condition	0.021	F(2,50)=0.134, p=0.876
VTA - NAcc (R) * gamble condition	0.143	F(2,50)=0.921, p=0.405
VTA - NAcc (L) * gamble condition	0.257	F(2,50)=1.660, p=0.200

*$p<0.05$

Table S2. Related to Figure 1.
Uncinate fasciculus and amygdala-NAcc tract fractional anisotropy (FA) were included as covariates of no-interest in all regression analyses involving the right AIns-NAcc tract. All results remained statistically significant or marginally significant, while neither of the control tracts were significantly correlated with positive skew preference and NAcc activity. Coefficient estimates are standardized **β**s. The uncinate fasciculus was tracked using Automated Fiber Quantification (AFQ; Yeatman et al., 2012). The amygdala-NAcc tract was tracked using the same methods described in *Experimental Procedures*. The amygdala VOI for seeding in tractography was defined by FreeSurfer segmentation (Fischl et al., 2002).

Association	**Variable of interest**
AIns-NAcc FA ~ Age + Uncinate fasciculus FA + Amygdala-NAcc FA	Age: **β**=0.56**, p=0.001
Positive skew preference ~ AIns-NAcc FA + Uncinate fasciculus FA + Amygdala-NAcc FA	AIns-NAcc: **β**=-0.36*, p=0.039
NAcc activity ~ AIns-NAcc FA + Uncinate fasciculus FA + Amygdala-NAcc FA	AIns-NAcc: **β**=-0.32†, p=0.072

**p<0.01, *p<0.05, †<0.10

Table S3. Related to Table 1.
Including left hemisphere neural activity did not improve model fit (as indexed by AIC, BIC, and a likelihood-ratio test: $\chi^2(3)=1.52$, $p=0.68$) for logistic regression models predicting behavior (subjects included as random effects).

Variables	Contrasts	Right VOIs model	Left VOIs model	Bilateral VOIs model
Previous Gamble	Win > Loss	-2.55* [-0.17, 0.07]	-2.35* [-0.15, 0.06]	-2.54* [-0.17, 0.07]
	Accept > Reject	2.01* [0.18, 0.09]	1.96* [0.17, 0.09]	2.05* [0.18, 0.09]
Domain of current earnings	Loss	1.71 [0.45, 0.26]	1.58 [0.42, 0.26]	1.70 [0.45, 0.26]
	Gain	1.52 [0.39, 0.26]	1.39 [0.36, 0.26]	1.51 [0.39, 0.26]
Skewness	Positive > Negative	5.50*** [0.32, 0.06]	5.73*** [0.34, 0.06]	5.44*** [0.32, 0.06]
	Skewed > Symmetric	-5.86*** [-0.52, 0.09]	-5.92*** [-0.52, 0.09]	-5.90*** [-0.52, 0.09]
Right NAcc		5.09*** [0.67, 0.13]		3.01** [0.54, 0.18]
Right AIns		-3.00** [-0.36, 0.12]		-2.91** [-0.38, 0.13]
Right MPFC		3.50*** [0.34, 0.10]		2.01* [0.28, 0.14]
Left NAcc			3.87*** [0.49, 0.13]	1.09 [0.19, 0.17]
Left AIns			-0.72 [-0.11, 0.15]	-0.22 [-0.04, 0.16]
Left MPFC			2.49** [0.22, 0.09]	0.54 [0.07, 0.14]
Pseudo R^2		0.30	0.29	0.30
AIC		2594	2612	2599
BIC		2657	2675	2679

Z-scores with coefficient estimates and SE in parentheses. ***p<0.001, **p<0.01, *p<0.05

Table S4. Related to Figure 3.
Additional mediation models verified that only right NAcc activity mediated the relation between right AIns-NAcc tract fractional anisotropy (FA) and positive skew preference. Path coefficients are standardized **β**s.

	a Structure ➞ Function	b Function ➞ Behavior	c'/c Structure ➞ Behavior
R AIns-NAcc FA ➞ R NAcc ➞ Positive-Skew	-0.35* (p=0.03)	0.46** (p<0.01)	c'=-0.24 (p=0.14) c=-0.40* (p=0.02)
R AIns-NAcc FA ➞ R AIns ➞ Positive-Skew	-0.07 (p=0.63)	0.12 (p=0.52)	c'=-0.39* (p<0.01) c=-0.40* (p=0.02)
R AIns-NAcc FA ➞ R MPFC ➞ Positive-Skew	-0.38* (p=0.01)	0.19 (p=0.28)	c'=-0.33* (p=0.03) c=-0.40* (p=0.02)
R MPFC-NAcc FA ➞ R NAcc ➞ Positive-Skew	-0.18 (p=0.27)	0.52*** (p<0.001)	c'=-0.10 (p=0.55) c=-0.19 (p=0.29)
R MPFC-NAcc FA ➞ R MPFC ➞ Positive-Skew	-0.21 (p=0.22)	0.28 (p=0.09)	c'=-0.14 (p=0.45) c=-0.19 (p=0.29)

***p<0.001; **p<0.01; *p<0.05

Supplemental Experimental Procedures

Reliability of risk preferences.

To verify the temporal stability of gamble choice as a measure of individual differences in risk preferences, we calculated the reliability of choices for each gamble condition across the experiment (see *Figure S2* and *Experimental Procedures*). Split-half reliability estimates indicated significant internal consistency in risk preference within each gamble condition and overall (positive-skew: ICC=0.89, $p<0.0001$; symmetric: ICC=0.91, $p<0.0001$; negative-skew: ICC=0.93, $p<0.0001$; overall: ICC=0.94, $p<0.0001$).

FMRI analysis.

For preprocessing, individual subject data were sinc interpolated to correct for non-simultaneous slice acquisition, corrected for motion in six dimensions, spatially smoothed using a small kernel (full width at half maximum=4 mm), and high-pass filtered (omitting frequencies with period < 90 s). Visual inspection of motion correction estimates confirmed that five subjects' heads had moved more than 2 mm in a plane from one whole-brain volume acquisition to the next, and these were excluded from further analysis.

To obtain activity time courses for targeted analyses, spherical volumes of interest (VOIs; 8 mm diameter) were centered on bilateral foci for the NAcc (Talairach coordinates: +/10,12,-2), AIns (Talairach coordinates: +/-34,24,-4), and MPFC (Talairach coordinates: +/-4,45,0), based on previous literature (Genevsky et al., 2013; Knutson and Greer, 2008). VOIs were warped from Talairach space to subjects' native brain space, and activity was spatially averaged within each VOI and then divided by the mean activity over the entire experiment to derive continuous measures of percent signal change. Time courses were then lagged 2 volume acquisitions (or 4 s) to account for the hemodynamic response delay to peak response.

DWI analysis.

For preprocessing, anatomical landmarks were manually defined in the anterior and posterior commissures (AC-PC), and the midsagittal plane to guide a rigid-body transformation that converted the T1-weighted images into AC-PC aligned space. Eddy-current distortions and subject motion in the diffusion-weighted images were corrected by a 14-parameter constrained non-linear co-registration based on expected eddy-current distortions, given the phase-encode direction of acquired data. Each diffusion-weighted image was registered to the mean of the motion-corrected non-diffusion-weighted (b = 0) images. The mean of the non-diffusion-weighted images was aligned to the T1 image in AC-PC space using a rigid body transformation. All raw diffusion images were resampled to 2 mm isotropic voxels by combining motion correction, eddy-current correction, and anatomical alignment into one general transformation, and then resampling the data using a seventh-order b-spline algorithm. Preprocessing was performed using the open-source mrDiffusion package (www.github.com/vistalab/vistasoft).

To define anatomical VOIs, each subject's AC-PC aligned T1-weighted image was processed with FreeSurfer software (http://surfer.nmr.mgh.harvard.edu/, Fischl, 2012). NAcc VOIs were identified from probabilistic subcortical tissue classification based on a manually labeled training set (Fischl et al., 2002). AIns VOIs were derived from the Destrieux cortical parcellation atlas, by combining the anterior insula and short gyrus parcellations (Destrieux et al., 2010). A binary mask was formed using the white versus gray-matter border identified by FreeSurfer to restrict fibers to the white-matter volume. To track previously described tracts of interest, spherical VOIs (8 mm diameter) were manually placed in bilateral MPFC and VTA, as described in previous research (Samanez-Larkin et al., 2012).

Probabilistic tractography.

Fiber tracking between AIns and NAcc VOIs was performed using constrained spherical deconvolution based probabilistic tracking, as implemented in MRtrix software (Tournier et al., 2007). The maximum number of harmonics was set to 10 (L_{max}=10), which defined the maximum number of deconvolution kernels utilized by constrained spherical deconvolution to estimate the fiber orientation distribution function in each voxel. This required 66 parameters for fitting the function (or 30 less than the 96 measured diffusion directions). Fiber pathways were generated by randomly seeding a voxel in a starting VOI and tracking until the fiber reached the ending VOI (step size=0.2 mm; minimum length=10 mm; maximum length=200 mm; minimum radius of curvature=1 mm; FA amplitude cutoff = 0.075; initial cutoff = 0.05). Fibers leaving the white-matter volume were discarded. Fiber tracking was also conducted on previously described mesolimbic tracts of interest between MPFC and NAcc VOIs, as well as VTA and NAcc VOIs (Samanez-Larkin et al., 2012). To ensure comparability with previous research, the same probabilistic tractography algorithm was again used to track these pathways in the current study (ConTrack; Sherbondy et al., 2008). A set of 50,000 candidate fibers connecting the VOI pairs were identified in each hemisphere. Seeds were placed randomly in both VOIs to ensure symmetric tracking. Candidate fibers were scored

using the ConTrack scoring algorithm, and the top-scoring 1% (which putatively tracked the most likely connecting pathways) were retained.

Fibers obtained from all tractography solutions were reduced to core fiber bundles by eliminating outliers and anatomically unlikely pathways (e.g., fibers crossing the cerebral hemispheres). Specifically, fibers greater than 2 standard deviations from the mean fiber length were initially removed. Fibers greater than 3 standard deviations away from the mean position of the core fiber (Mahalanobis distance) were then removed. Finally, fibers that crossed the midsagittal plane or took indirect routes between VOIs were removed (e.g., those that projected in one direction, but then looped backward). The proportions of fibers removed from each tract, averaged across subjects, were: right AIns-NAcc: 0.61, left AIns-NAcc: 0.54, right MPFC-NAcc: 0.31, left MPFC-NAcc: 0.30, right VTA-NAcc: 0.61, left VTA-NAcc: 0.62. These proportions were similar to the proportion of fibers discarded for previously characterized tracts using the same method (e.g., right uncinate: 0.59, left uncinate: 0.64, right amygdala-NAcc: 0.49, left amygdala-NAcc: 0.47; see also *Figure S1*).

Tract validation.

Linear Fascicle Evaluation (LiFE) is a forward modeling approach that predicts the raw measured diffusion signal by generating a synthetic signal using all of the discovered fascicles in the white-matter brain volume. A weight is assigned to each fascicle in a connectome by computing the root mean squared error difference between measured and predicted signal. Many fascicles are deleted during this process and not considered for further anatomical analysis. To statistically validate surviving fascicles, those forming a tract of interest (e.g., the AIns to NAcc tract) are removed from the connectome by a "virtual lesion". The resulting "lesioned" connectome should have increased root mean squared error, which can be compared to the error of the unlesioned connectome. The strength of evidence in favor of a tract is measured as the increase in root mean squared error between the lesioned and unlesioned connectome. Thus, this analytic procedure shares similarity with power analysis and can quantify the statistical evidence for a specific tract, given the measured whole brain diffusion signal and the estimated fascicles.

To validate tracts of interest, we first tracked a whole-brain connectome by applying the same parameters used for the AIns to NAcc tract to a whole-brain seed mask. Next, we specifically evaluated the difference in error in the set of voxels that intersected with the tract of interest. Fascicles from the whole-brain connectome that passed through at least one of the voxels were designated as path-neighborhood fascicles (Wedeen et al., 2012; *Figure S1*). We calculated the root mean squared error of the predicted diffusion signal in each voxel using the full unlesioned model (including path-neighborhood and tract of interest fascicles), as well as root mean squared error for a reduced model (a virtual lesion model that included only the path-neighborhood fibers). The strength of the evidence favoring the existence of a tract of interest was calculated as the difference in the full minus reduced model mean prediction errors (μ) divided by their pooled standard deviations (**Figure 1B**).

The strength of evidence (*S*) returns a scalar value bounded at zero and infinity. We used this value for group statistics across individual brains, and tested that the mean strength of evidence (*S*) was greater than zero (methods detailed in Gomez et al., 2015; Pestilli, 2015, Pestilli et al., 2014, and Takemura et al., 2015; francopestilli.github.io/life).

For identified tracts, one-sample Wilcoxon signed-rank tests compared the mean strength of evidence (log-transformed to unbound the distribution of values from $-\infty$ to $+\infty$) against the null hypothesis of no evidence for the tracts ($\mu = 0$), and indicated significant strength of evidence for all tracts (right AIns-NAcc: $V=528$, $p<0.001$; left AIns-NAcc: $V=523$, $p<0.001$; right MPFC-NAcc: $V=528$, $p<0.001$; left MPFC-NAcc: $V=528$, $p<0.001$; right VTA-NAcc: $V=528$, $p<0.001$; left VTA-NAcc: $V=471$, $p<0.001$; see also *Figure S1*).

Diffusion index calculation.

Diffusion properties of validated tracts were characterized by obtaining mean fractional anisotropy (FA) for each tract, which can vary as a function of fascicle density, axon diameter, and myelination. To assess variation in FA along the trajectory of each tract, we spatially normalized fiber pathways between subjects by sampling 100 evenly spaced cross-sectional nodes along the tract length from the starting VOI to the ending VOI. The mean FA in each node was then calculated as an average of each fiber's FA in that node, weighted by the spatial distance of that fiber from the node's core fiber. We then averaged FA across the middle 50% of nodes along each pathway to ensure that FA measures exclusively included white matter, but not voxels along the gray versus white-matter boundary. This generated a single FA (or "coherence") value for each tract in each hemisphere of every subject (see also Yeatman et al., 2012). These measures robustly correlated across hemispheres (AIns-NAcc: $r=0.59$, $F(1,30)=15.89$, $p<0.001$; MPFC-NAcc: $r=0.79$, $F(1,30)=50.89$, $p<0.001$; VTA-NAcc: $r=0.82$, $F(1,30)=61.01$, $p<0.001$).

Replication and extension of previously identified associations of tract coherence with age.

Results from this new dataset replicated a previously documented negative association of age with bilateral MPFC-NAcc tract coherence (β=-0.53, $t(30)=-3.42$, $p=0.002$), as well as a marginally positive association of age with

bilateral VTA-NAcc tract coherence (**β**=0.35, t(30)=2.03, p=0.051; see **Figure 1D** in main paper; Samanez-Larkin, et al., 2012). Like VTA-NAcc tract coherence, age was positively associated with AIns-NAcc tract coherence in both hemispheres, (right: **β**=0.42, t(30)=2.52, p=0.02; left: **β**=0.45, t(30)=2.79, p=0.01; bilateral: **β**=0.49, t(30)=3.07, p=0.005; all coefficient estimates are standardized).

These findings also replicated specific age correlates of the coherence of these tracts, since MPFC to NAcc tract coherence was negatively correlated with age, but projections connecting the midbrain and the NAcc were not (Samanez-Larkin et al., 2012). Interpreting the properties of mesolimbic midbrain to NAcc projections poses a challenge than putative unidirectional glutamatergic MPFC to NAcc and AIns to NAcc projections, since the mesolimbic tract contains neurochemically varied and bidirectional projections traversed by numerous crossing fibers (Nieuwenhuys, 1985). Nonetheless, several reports using diffusion weighted tractography have now traced the trajectory of mesolimbic projections (Bracht et al., 2014; Coenen et al., 2012; Samanez-Larkin et al., 2012), and future combination with comparative techniques may better disentangle contributions of different components of this tract (e.g., Lammel et al., 2011). As with the midbrain to NAcc tract, age was positively correlated with the coherence of the AIns to NAcc tract. While unexpected, this association deserves further replication and exploration, particularly with respect to physiological mechanisms responsible for age-related decreases in the coherence in prefrontal but not subcortical tracts, their plasticity, and implications for function.

Distinguishing alternative tracts.

Since the AIns-NAcc tract and uncinate fasciculus share a proportion of voxels in some (but not all) subjects, the current methods cannot dissociate their diffusion characteristics in intersecting voxels. To partially address this issue, fractional anisotropy of the uncinate fasciculus was assessed and included as a covariate in all regressions involving the right AIns-NAcc tract, but could not statistically account for the results (see *Table S2*). The nearby ventral amygdalofugal pathway connecting the amygdala to the NAcc was also tracked using the current methods, and shown to terminate in posterior NAcc without intersecting with the more anterior AIns-NAcc tract (see *Figure S1*). The amygdala-NAcc tract also courses through the uncinate fasciculus, following the same superior trajectory as the uncinate in the inferior temporal cortex (Petrides and Pandya, 2007), but then diverging medially near the edge of the insula. These amygdalar projections are considered as distinct from the uncinate tract (Ungerleider, Gaffan, and Pelak, 1989). Amygdala-NAcc tract fractional anisotropy was also included with uncinate fractional anisotropy as a covariate in all regressions, and similarly could not statistically account for the AIns-NAcc tract results (see *Table S2*). Together, these additional analyses suggest that the AIns-NAcc tract is at least partially distinct from other nearby tracts, but further verification of this distinction will have to await the development of more sophisticated methods for teasing apart different but overlapping tracts.

Supplemental References

Bracht, T., Doidge, A. N., Keedwell, P. A., and Jones, D. K. (2015). Hedonic tone is associated with left superflo-lateral medial forebrain bundle microstructure. *Psychol Med*, *45*, 865-874.

Destrieux, C., Fischl, B., Dale, A., and Halgren, E. (2010). Automatic parcellation of human cortical gyri and sulci using standard anatomical nomenclature. *NeuroImage*, *53*(1), 1–15.

Fischl, B. (2012). FreeSurfer. *Neuroimage*, *62*(2), 774-781.

Fischl, B., Salat, D.H., Busa, E., Albert, M., Dieterich, M., Haselgrove, C., van der Kouwe, A., Killiany, R., Kennedy, D., Klaveness, S., Montillo, A., Makris, N., Rosen, B., and Dale, A.M. (2002). Whole brain segmentation: automated labeling of neuroanatomical structures in the human brain. *Neuron*, 33, 341-355.

Genevsky, A., Västfjäll, D., Slovic, P., and Knutson, B. (2013). Neural underpinnings of the identifiable victim effect: affect shifts preferences for giving. *The Journal of Neuroscience*, *33*(43), 17188–17196.

Gomez, J., Pestilli, F., Witthoft, N., Golijeh, G., Liberman, A., Poltoratski, S., Yoon, J., and Grill-Spector, K. (2015). Functionally defined white matter reveals segregated pathways in human ventral temporal cortex associated with category-specificity. *Neuron*, *85*(1), 216–227.

Lammel, S., Ion, D. I., Roeper, J., and Malenka, R. C. (2011). Projection-specific modulation of dopamine neuron synapses by aversive and rewarding stimuli. *Neuron*, *70*(5), 855-862.

Mai, J.K., Assheuer, J., Paxinos, G. (1997). Atlas of the human brain (San Diego: Academic Press).

Nieuwenhuys, R. (1985). Chemoarchitecture of the Brain. SpringerVerlag, New York.

Pestilli, F. (2015). Test-retest measurements and digital validation for in vivo neuroscience. *Scientific Data*, *2*, 140057.

Petrides, M., and Pandya, D.N. (2007). Efference Association Pathways from the rostral Prefrontal Cortex in the Macaque Monkey. *The Journal of Neuroscience*, 27(43): 11573-11586.

Sherbondy, A.J., Dougherty, R.F., Ben-shachar, M., and Wandell, B.A. (2008). ConTrack: Finding the most likely pathways between brain regions using diffusion tractography. *Journal of Vision*, *8*(9), 1-16.

Takemura, H., Rokem, A., Winawer, J., Yeatman, J.D., Wandell, B.A., and Pestilli, F. (2015). A major human white matter pathway between dorsal and ventral visual cortex. *Cerebral Cortex*, published online March 31, 2015, doi: 10.1093/cercor/bhv064

Ungerleider, L.G., Gaffan, D., and Pelak, V.S. (1989). Projections from the inferior temporal cortex to prefrontal cortex via the uncinate fascicle in rhesus monkeys. *Experimental Brain Research*, 76: 473-484.

Wedeen, V.J., Rosene, D.L., Wang, R., Dai, G., Mortazavi, F., Hagmann, P., Kaas, J.H., and Tseng, W.I. (2012). The geometric structure of the brain fiber pathways. *Science*, *335*(6076), 1628-1634.